Anthony Marin*, Ravi Kishore, Darian A. Schaab, Dusan Vuckovic and Shashank Priya

Micro Wind Turbine for Powering Wireless Sensor Nodes

DOI 10.1515/ehs-2013-0004

Abstract: The goal of this study was to design a micro wind turbine having dimensions on the order of 1–10 cm^3 for powering wireless sensor nodes. Using the parametric study based upon a computational model, the coupling factor between the blade and generator section was significantly enhanced. Building upon the formulation for the coupling factor, we derived efficiency metric for the rotational generators. A prototype was designed based upon the analytical study conducted through the combination of blade element momentum theory and ANSYS magnetics to match the performance of the generator to that of the blades. The blade diameter and depth was 72 mm and 9 mm, respectively. The generator diameter was 26 mm with total volume of 18.1 cm^3. It was found that the micro wind turbine generated DC output power of 12.39 mW, 49.03 mW and 102.61 mW at 3.7 m/s, 6 m/s and 8 m/s wind speeds, respectively. The power density was computed to be 0.304, 1.204, and 2.52 mW/cm^2, respectively, which are higher than all the other results reported in the literature.

Keywords: wind energy harvesting, wireless sensor node, permanent magnet generator

***Corresponding author: Anthony Marin,** Center for Energy Harvesting Materials and Systems (CEHMS), Virginia Tech, Blacksburg, VA 24061, USA; Bio-Inspired Materials Development Laboratory (BMDL), Virginia Tech, Blacksburg, VA 24061, USA, E-mail: marinvt@gmail.com

Ravi Kishore, Center for Energy Harvesting Materials and Systems (CEHMS), Virginia Tech, Blacksburg, VA 24061, USA; Bio-Inspired Materials Development Laboratory (BMDL), Virginia Tech, Blacksburg, VA 24061, USA

Darian A. Schaab, Center for Energy Harvesting Materials and Systems (CEHMS), Virginia Tech, Blacksburg, VA 24061, USA; Bio-Inspired Materials Development Laboratory (BMDL), Virginia Tech, Blacksburg, VA 24061, USA; Technische Universität Darmstadt, Darmstadt, Germany

Dusan Vuckovic, IdemoLAB, DELTA, Hørsholm, Denmark/Technical University Denmark, Lyngby, Denmark

Shashank Priya, Center for Energy Harvesting Materials and Systems (CEHMS), Virginia Tech, Blacksburg, VA 24061, USA; Bio-Inspired Materials Development Laboratory (BMDL), Virginia Tech, Blacksburg, VA 24061, USA

1 Introduction

Recently, there has been significant focus on reducing the energy demand of commercial buildings that utilize almost 20% of the total energy consumed within the United States (Accessed July 28, 2013. http://energy.gov/articles/energy-department-invests-save-small-buildings-money-saving-energy). As a result, the need for "smarter" buildings has grown that can reduce the amount of wasted energy. One attribute of smart buildings includes utilizing the remote sensors that sense the occupancy and human activity and intelligently adjust the lights and other electrical loads. These sensors require power in the range of 1–10 mW which needs to be accomplished through batteries or grid electricity. Batteries have a limited lifetime and thus they have to be replaced regularly. Wiring each sensor to the grid electricity is not only cumbersome but also cost prohibitive. A promising solution to this end, is harvesting the wind energy available from HVAC ducts. This solution addresses both the problems, as it provides power for prolonged period of time and it does not require extended wiring as the sensor can be integrated within the wind harvester.

Prior researchers have investigated the feasibility of powering a wireless sensor utilizing the HVAC flow through micro wind turbines. Flammini et al. combined the commercially available brushless servomotors from Portescap and a DC servomotor from Faulhaber with commercially available six turbine blades having a diameter of 4 cm. They were able to demonstrate a maximum DC power of 36 mW at a wind speed of 9 m/s which implies the system efficiency of 6% (Flammini and Marioli 2010). Federspiel et al. have reported a similar prototype that achieved efficiencies up to 11% (Federspiel and Chen 2003). Xu et al. utilized a 7.6 cm thorgren plastic propeller with four blades in combination with a MABUCHI sub watt brushless DC motor. They were able to model the system performance and further demonstrated power generation of 18 mW at a wind speed of 4 m/s (Xu et al. 2010). Howey et al. were able to match the Blade Element Momentum theory considerations with the experimental results of their blades. They designed a 2 cm rotor with custom built generator. At wind speeds of 3 m/s they harvested 80 μW, which is equal to an overall

efficiency of 0.61%, and their turbine reached a power coefficient up to 9% (Howey et al. 2011). Several researchers have also focused on the circuitry, which has to overcome the problem of fluctuating wind speed and perform signal processing to provide output that is compatible with the low power electronics. Keng et al. introduced an active rectifier using a MOSFET for low power amplitudes as well as a maximum power tracking technology (MPPT) to adapt the load on the turbine to the maximum power point (Yen Kheng and Panda 2011). Carli et al. built a 6.3 mW turbine which was capable of producing 10 mW at a wind speed of 4.44 m/s. Their prototype incorporated a buck-boost converter that was capable of tracking the maximum power point of the turbine (Carli et al. 2010). Few researchers have also proposed their own generator design. Holmes et al. discussed the advantages of using an axial-flux permanent magnet for low power wind energy harvesting. These generators have large coupling factors and low stall torque (Holmes, Hong, and Pullen 2005).

This study addresses the design and optimization of a micro wind turbine system utilizing a combination of finite element analysis and analytical models. The blades for the turbine were optimized with BEM theory for a marginal wind speed of 3 m/s and the generator was designed as axial-flux configuration. Our work was focused on enhancing the coupling between the mechanical and electrical systems and ultimately refining the key design parameters of the generator to increase the overall efficiency. An optimized prototype was fabricated that surpasses the state-of-the-art in power density for micro wind turbines. In addition, maximum power point tracking circuit with energy management was developed and characterized. The complete system was combined with a radio and a PIR sensor to demonstrate the capabilities of the self-powered sensing.

2 Micro Wind Turbine Design

The dimension and structure of the wind energy harvester prototype is shown in Figure 1(a) with the top half of the generator housing removed to reveal the internal components. The back and front view of the blades can be seen in Figure 1(b)–(c). BEM theory was used to optimize the blade geometrical parameters such as twist angle, chord length, number of blades, and solidity. The optimized flat

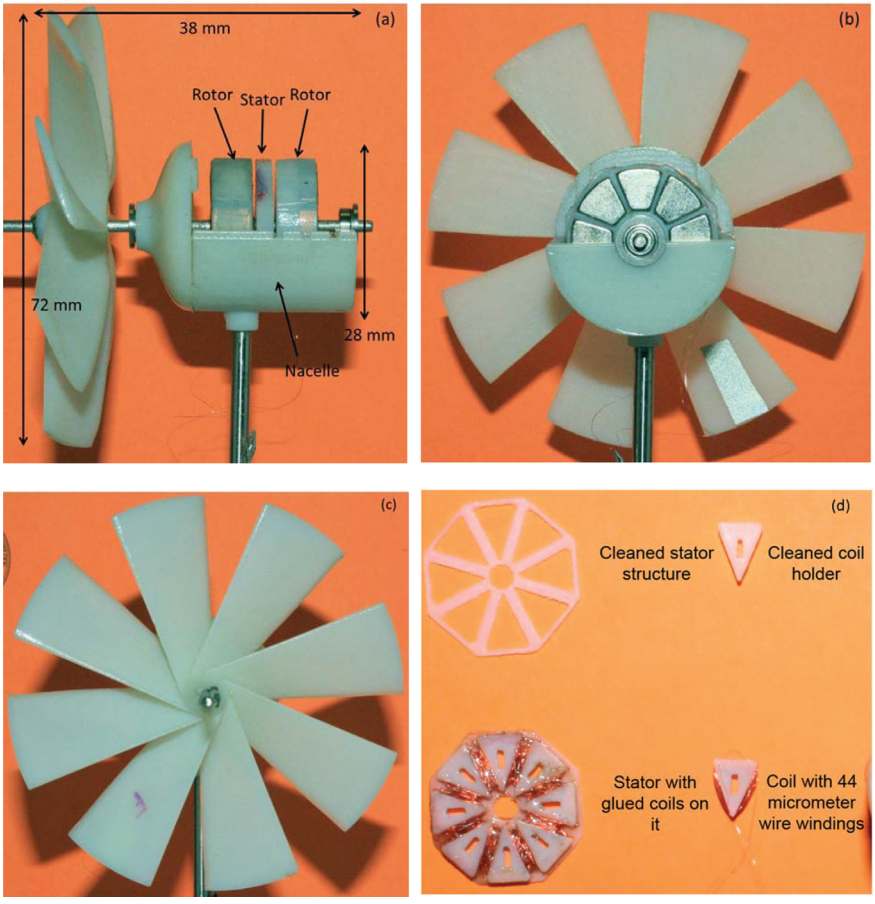

Figure 1: (a) Side-view of micro wind turbine prototype with dimensions, (b) back-view, (c) front-view, (d) Internal coil layout inside stator casing.

blade had a maximum predicted coefficient of performance of 0.207 as compared to the airfoil the coefficient that was only 0.18, therefore a flat blade profile was utilized for this study. The blade profile had a total diameter of 72 mm and consisted of 8 individual blades. The angle of attack was 5°, taper angle was 12°, and the solidity was 0.7. As shown in Figure 1(d), the ABS plastic stator in the generator houses eight copper wire wound coils with a fill factor of 71.3% and having a total resistance of 1,984 Ω. The shape of each coil was designed to match the shape of the magnetic field distribution in order to maximize the mechanical to electrical energy conversion thereby increasing the overall efficiency of the prototype. The total diameter of the circular stator was 22 mm and the thickness was 2.65 mm (coil – 1.25 mm, ABS plastic – 1.4 mm).The generator rotor houses eight arc shaped magnets of dimension 10.55 mm outer radius × 4.2 mm inner radius × 6.35 mm thickness (42^{o} between the two edges). The neodymium iron boron permanent magnets (B4201 K&J magnetics) were arranged in a circular array with adjacent magnets having alternate polarity. Opposite polarity exists between adjacent magnets to allow for series connection of all the eight coils. The air gap between the two rotors was 4.05 mm.

An electronic circuit that maximized the efficiency of the power transfer between the micro wind turbine and wireless sensor was also developed. The electronic circuit was divided into three main parts: (i) The AC/DC section with maximum power point control; (ii) the energy management; (iii) the sensing stage. In the first part, the output of the micro wind turbine was rectified and forwarded to the input of the DC/DC converter. The converter was designed so it matched the impedance of the micro wind mill turbine's output at the expected wind speed in the HVAC duct. This resulted in maximized power transfer between the micro wind mill turbine and the energy management. The energy management stage controls the routing of the power between different parts of the system and stores the generated excess power in a supercapacitor for later use. The sensing stage consists of the sensor and the wireless communication block that relays the data generated by the sensor to the base station, where the information can be later used for building automation.

3 Computational Model for the Micro Wind Turbine Harvester

In order to model the micro wind turbine system, the relationships between the angular velocity and torque for both the blade and generator were determined as these relationship couple the two parts of the overall systems. The relationship between the wind speed and blade torque and the wind speed and angular velocity were determined by Blade Element Momentum modeling. BEM modeling consists of a 2D mathematical analysis of the 3D flow of air around the wind turbine blades. The model utilizes coefficients of drag and lift from a program called XFLR5 v6.06 (www.xflr5.com) for a given blade profile, and predicts the power coefficient vs tip speed ratio relationship. The relationship between the angular velocity and generator torque can then be derived. A detailed description of the BEM analysis can be found in the following references (Burton 2001; Manwell, McCowan, and Rogers 2006). To model the generator portion of the micro wind turbine, ANSYS FEA was utilized to estimate the transformation factor, Φ, which directly couples the mechanical energy to electrical energy. The effect of the magnitude of the electrical load was also modeled and a metric for characterizing the efficiency of rotational generators is described.

3.1 Magnetic-Nodal Analysis of the Magnetic Circuit

The spatial distribution of magnetic flux through the coil was simulated in ANSYS and used to estimate the transformation factor ($\Phi_{\max}$), a procedure which is described in detail in Refs (Marin 2013; Marin et al. 2011). As the current in the AC generator varies with time an approximation is made that this variation is sinusoidal in order to formulate the average torque and average power terms. The assumption was verified by implementing the generator geometry in ANSYS Maxwell. Figure 2(b) displays the waveform that was generated using the geometry specified in Figure 2(a).

Through simulation of the generator, the maximum power delivered to the electrical domain occurs when $R_L = R_c$. However, the usable power that can be extracted across an electrical load is only 50% of the total electrical power in the electrical domain. Therefore, we derive the equation for maximum power delivered to an electrical load and provide a simple method to compare the generator efficiency for wind turbine in general. Applying Kirchoffs's voltage law to the magnetic circuit, the following relationship for current delivered to a load can be derived:

$$\Phi(t) r \dot{\theta} - (R_e + R_L) i(t) = 0 \qquad [1]$$

Where $\Phi(t)$ is the transformation as a function of time, r is a normalized radius to which magnetic field values are reference from (0.01 m for this work), $\dot{\theta}$ is the angular

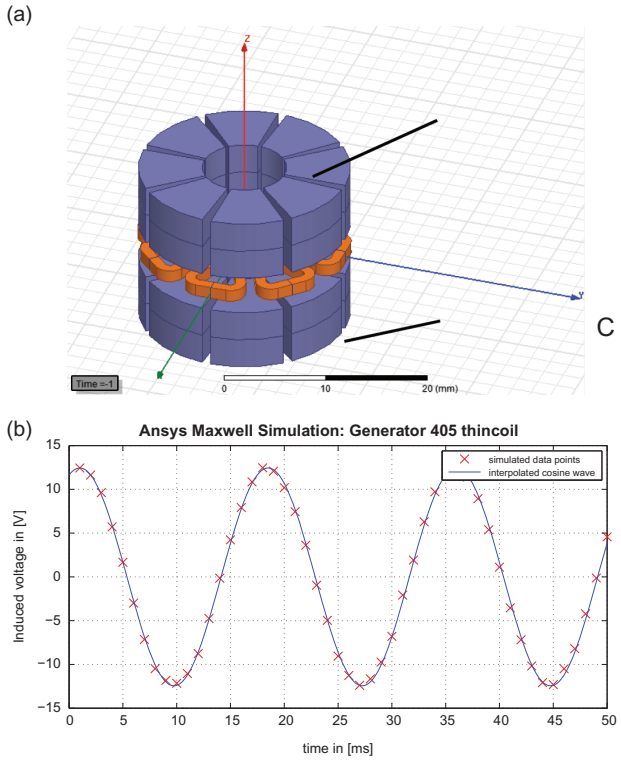

Figure 2: (a) Geometry simulated in ANSYS Maxwell and (b) Output voltage from simulation.

velocity of the generator, R_e is the resistance of the induction coil, R_L is the load resistance.

$$i(t) = \frac{\Phi(t) r}{R_e + R_L} \dot{\theta} \quad [2]$$

where power delivered to electrical domain can be expressed as:

$$P_{elec}(t) = i(t)^2 (R_e + R_L) \quad [3]$$

and usable power delivered to an electrical load is given as:

$$P_{load}(t) = i(t)^2 R_L \quad [4]$$

$$P_{avg,\,load} = \frac{\Phi_{\max}{}^2 r^2 \dot{\theta}^2}{2(R_e + R_L)^2} R_L \quad [5]$$

where generator efficiency can be defined as:

$$\eta = \frac{P_{load}}{P_{elec}} = \frac{i(t)^2 R_L}{i(t)^2 (R_e + R_L)} = \frac{R_L}{R_e + R_L} = \frac{1}{1 + \frac{R_e}{R_L}} \quad [6]$$

Enhancing the efficiency of the generator by increasing the coupling Φ also increases the generator torque and decreases the angular velocity of blades and shaft. The generator torque which opposes the torque generated by the wind passing over the blades is governed by the following equation:

$$\begin{aligned} \tau_{generator,\,avg} &= F_{avg} r_{gen} = \frac{\Phi_{\max}}{\sqrt{2}} I(t) r_{gen} \\ &= \Phi_{\max} \frac{\Phi_{\max}}{2(R_e + R_L)} r_{gen}{}^2 \dot{\theta} \\ &= \frac{(\Phi_{\max})^2 r_{gen}{}^2}{2(R_e + R_L)} \dot{\theta} \end{aligned} \quad [7]$$

The incoming torque from the blades varies with the angular velocity, therefore, the generator in turn affects the available power. For this reason a coupled model between the blades and the generator should be derived in order to enhance the overall efficiency of the micro wind turbine.

4 Experimental Setup

The micro wind turbine was experimentally characterized in an open jet wind tunnel with a square 0.7 m × 0.7 m test section developed in 2008 by members of the Virginia Tech Aerospace and Ocean engineering faculty and constructed in 2009. The fan discharges into a 6°, 4 m-long diffuser. The flow is then directed into a 1.47 m-high by 1.78 m-wide settling chamber. A combination of 0.01 m-cell size, 0.09 m long honeycomb followed by three turbulence reduction screens (made of 0.3 mm-diameter fiberglass screen with a 55% open area ratio) ensure a low turbulence and uniform flow. The flow then discharges in the atmosphere through a 5.5:1 contraction nozzle based on a 5th degree polynomial profile. To minimize the impact of the flow on the lab environment, the tunnel is equipped with a jet catcher located 1.2 m downstream of the contraction exit. The rotational velocity was measured using a Shimpo DT-209X tachometer in real time. Wind tunnel velocity was measured using an Xplorer GLX PS-2002 vane anemometer. Voltage generated by the wind turbine was measured by placing a load resistor in series with the coil. The RMS voltage was measured by using a digital multimeter. For DC voltage measurements a full bridge rectifier using Schottky diodes was placed on the output of the wind turbine. The torque was calculated from the measured velocity profile acquired from startup to steady state condition. The velocity profile was curve fitted and differentiated to obtain an acceleration curve. The acceleration curve was multiplied by the moment of inertia of the micro wind turbine rotating components. To calculate stall torque the curve was extrapolated to $t = 0$. The moment of inertia for the rotating components was calculated using SolidWorks and was found to be 3.023×10^{-7} kg.m^2. Figure 3 displays the picture of the experimental setup. Note the anemometer was not in position at the time of

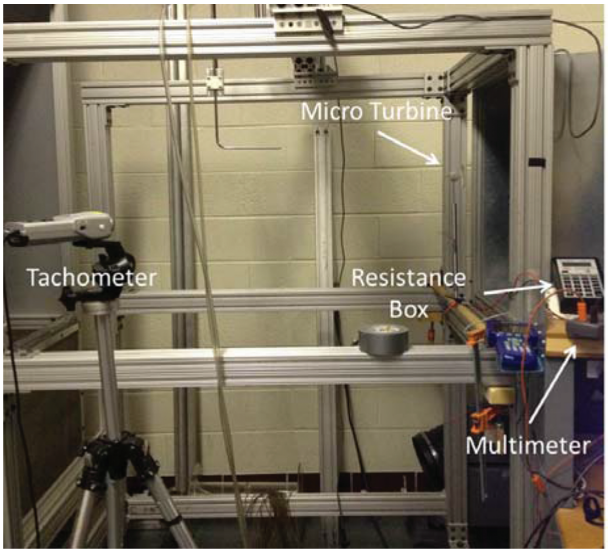

Figure 3: Wind tunnel characterization setup with tachometer, micro turbine, resistance box and multimeter at the open end of the wind tunnel.

the photograph however is placed at same height as micro wind turbine and towards the side of the exit. A small variation in flow velocity was measured between the position of the anemometer and micro wind turbine and was accounted for during experimentation.

5 Results and Discussion

The micro wind turbine was experimentally characterized at several different wind speeds ranging from 2 m/s to 12.5 m/s as these were the values identified for a typical commercial HVAC system. By applying the theory presented in the previous section to the experimental data, we validated the accuracy of the model. The theoretical performance for the blades at 3 m/s flow velocity is summarized in Figure 4(a)–(b). Figure 4(a) describes the coefficient of performance (C_p) as a function of the tip speed ratio (λ).We can convert the $C_p - \lambda$ relationship to blade power (available power for harvesting) vs. angular velocity relationship to understand how the generator should be designed in order to maximize the output power of the wind turbine and overall efficiency. Figure 4(b) displays the blade power and blade torque as a function of angular velocity suggesting that 13.7 mW of power is available from the generator at 125 rad/s with 0.11 mN*m of torque.

Utilizing the torque velocity relationships that were derived for both the blades and the generator we can simulate the optimum load resistance that leads to the highest efficiency. The relationship with blade torque was assumed to be linear and eq. [8] was generated from a linear curve fit of the blade torque – angular velocity trend as shown in Figure 4(b):

$$\tau_{blade} = -1.1e-6\omega + 0.00024 \quad [8]$$

Figure 5 displays the results of the simulation showing that across an optimum load resistance of 16 kΩ, about 10.86 mW of power is generated. This leads to a generator

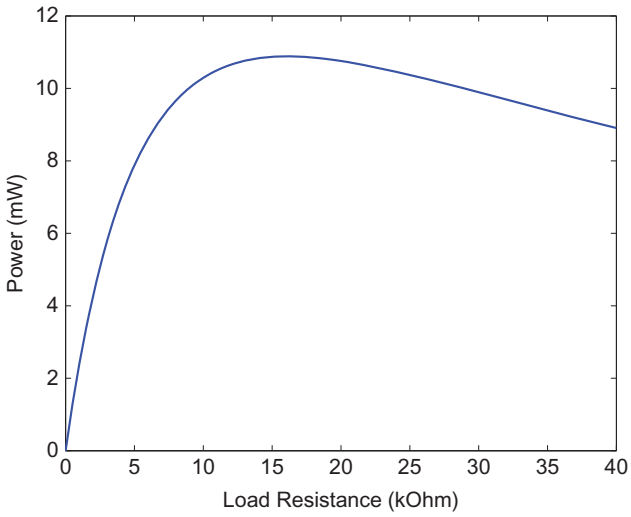

Figure 5: Power as a function of load resistance.

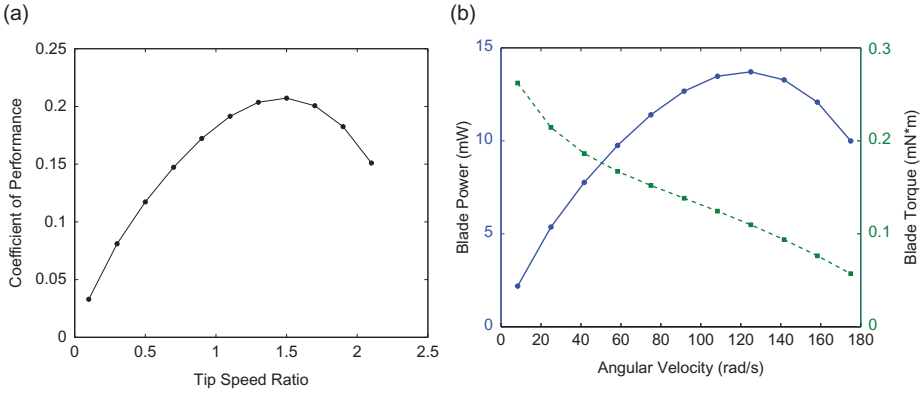

Figure 4: (a) Theoretical C_p vs TSR for 3 m/s wind speed, and (b) blade power and blade torque as a function of angular velocity at 3 m/s wind speed.

efficiency of 85.6%, combined system efficiency of 79.2%, and wind turbine efficiency of 16.4%.

The generator and system efficiency can be further enhanced by increasing the coupling term without increasing the resistance. As shown in eq. [6], the generator efficiency increases as the difference between the optimum load resistance and coil resistance increases. To maintain the same matched torque, eq. [7] shows that if Φ increases without an increase in the coil resistance, the optimum load resistance will increase. Therefore, a higher overall system efficiency can be achieved. The increase is limited as one cannot increase the coil size as the resistance is increased. The other possibility is to use thicker magnets which will increase the overall volume of the prototype. Another method to increase the coupling is to implement a gear train. Planetary gear trains can create a variety of different gear ratios in small compact volume. Figure 6(a) displays the results with implementation of gear train into the model showing that increasing the gear ratio increases the load resistance and therefore the power output. To analyze how much the output power increases with increase in the gear ratio, we plot power at optimum load resistance as a function of gear ratio in Figure 6(b). A 14.6% increase in power was gained from the addition of a 2:1 gear ratio and an additional increase of 2.8% in power was achieved from a 3:1 gear ratio. The increase hereafter is minimal (0.89%) and therefore is not recommended as increasing the gear ratio will increase the startup speed of the prototype. With a 3:1 gear ratio, 12.8 mW of power was generated at 120 kΩ optimum load. This leads to a generator efficiency of 97.8%, system efficiency of 93.4%, and wind turbine efficiency of 19.4%. These increases were computed by assuming no loss in efficiency due to the gearing. In future study, the effect of the gearing efficiency must be considered.

To validate the model, the results from the simulation were compared to the experimental results. Figure 7(a)–(b) displays the results of the blade power and torque vs. angular velocity that was determined experimentally. The experimental Cp and blade power were 21% lower than the theoretical predictions. This is due to the limitations of the BEM model as discussed in the analytical modeling section. Experimentally, it was determined that 10.81 mW of power was available to be harvested from blades with 3 m/s wind speed. Figure 7 (b) displays the blade power and blade torque vs. angular velocity relationship suggesting that 10.81 mW can be harvested with the generator at 85 rad/s with 0.123 mN*m of torque.

To validate the proposed model, eq. [9] was generated from a linear curve fit of the blade torque/angular velocity trend shown in Figure 7(b).

$$\tau_{blade} = -2.3e - 6\omega + 0.00034 \quad [9]$$

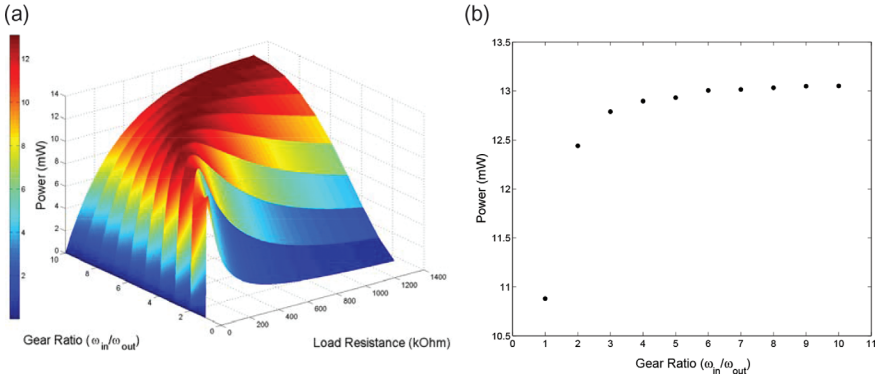

Figure 6: (a) Performance with implementation of gear train into the model showing that increasing gear ratio increases the load resistance and therefore the power output, and (b) power at optimum load resistance as a function of gear ratio.

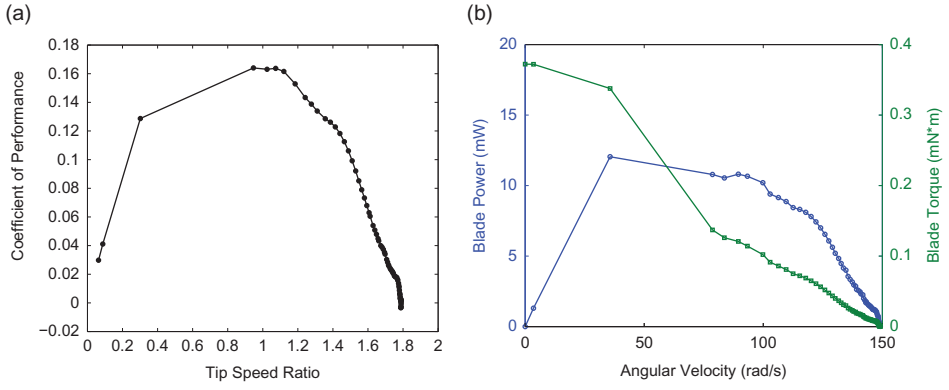

Figure 7: (a) Experimental Cp vs. TSR for 3 m/s wind speed, and (b) blade power and blade torque vs. angular velocity for 3 m/s wind speed.

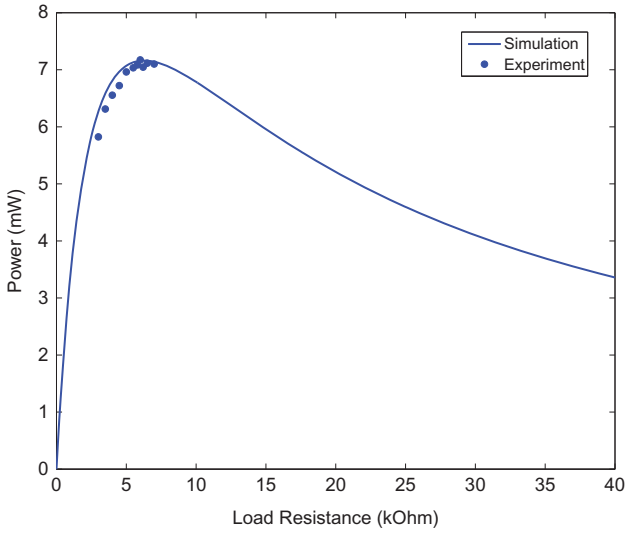

Figure 8: Model comparison with experiments using optimized generator.

Figure 8 displays the results of the simulation showing an optimum load resistance of 6 kΩ generating power of 7.17 mW. The experimental data and simulations were found to be in good agreement. The results show a generator efficiency of 69%, combined system efficiency of 66 %, and wind turbine efficiency of 10.8%.

Figure 9(a) displays the experimental and theoretical steady state angular velocities at the various wind speeds for the micro wind turbine. The theoretical blade torque vs. angular velocity was not used in the calculation. The relationship was determined from the experimental values in order to validate the mathematical formulation. The results were in reasonable agreement validating the mathematical models presented earlier. Figure 9(b)–(c) displays the experimental and theoretical power output of the wind turbine at five different wind speeds. The experimental results are in good agreement with the theoretical results.

Marin *et al.* have developed the generator based upon the computational model of the generator as described in the Marin (2013). The initial generator design had a magnetic rotor with a height of 3.175 mm and 9,600 windings (2,700 Ohms) and a gap of 5.25 mm. An electromagnetic coupling factor of $\Phi = 12.08 Vs/m$ was measured in the wind tunnel. This generator was used to validate the theory, which can be seen in Figure 9(a) to (c), and was discussed in the previous paragraph. To increase the efficiency, the generator has to apply a specific torque on the blades, while being connected to a load resistance that is higher than the coil resistance. A graphical progression of the efficiencies can be seen in Figure 10. Increasing the load resistance for a given prototype increases the generator efficiency and decreases the torque of the generator. This implies that the coupled system operates at lower blade efficiencies (on the left side of the COP curve). The optimized design had doubled height (6.35 mm) of the magnetic rotor and the same gap. This lead to an increased electromagnetic coupling factor of $\Phi = 16.99 Vs/m$, while having the same number of windings and a similar coil resistance. This higher coupling factor allowed increasing the load

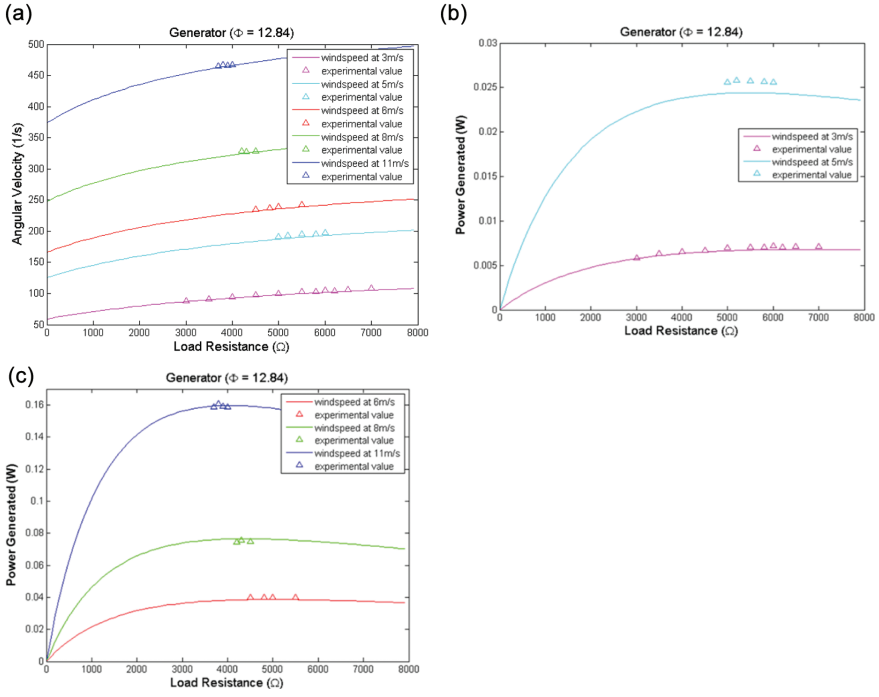

Figure 9: (a) Comparison of the predicted and experimental angular velocity, (b) Comparison of the predicted and experimental power generation at 3 and 5 m/s, and (c) Comparison of the predicted and experimental power generation at 6, 8 and 11 m/s.

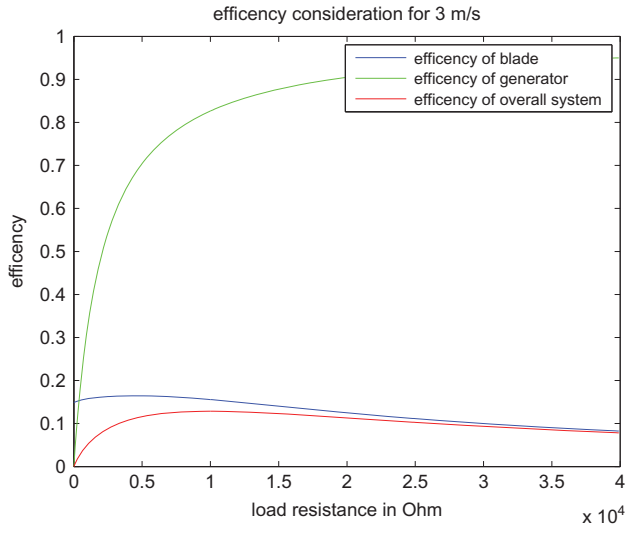

Figure 10: Efficiency plot of the blade, generator and the coupled system. Decreases in coil resistance, while keeping the electromagnetic coupling factor of the generator constant, shifts the green curve towards the left and increases the overall efficiency.

resistance, as the torque from the generator stays constant. This increased the generator efficiency and thus the overall system efficiency.

The gap between the rotors influences the two main design parameters of the generator. The magnetic field between the rotors increases with decreasing gap while the number of windings decreases and so does the coil resistance. Our simulations showed that both effects balance out, which allows to keep the same electromagnetic coupling factor, while decreasing the load resistance. This was addressed with the next variation of the generator. This design included the same double height magnetic rotor, 7,200 windings (1,984 Ohms) and a decreased gap of 4.05 mm. For this design a new cover box was developed to secure the wires from being scratched by the rotor. Through this design the electromagnetic coupling factor was further increased to a value of $\Phi = 18.68 Vs/m$, but at a lower coil resistance, which lead to our final system efficiency. Table 1 summarizes the performance of each generator developed throughout this study and Figure 11 compares the prototypes to the published literature showing that our prototype is state-of-the-art at all wind speeds.

6 Micro Wind Turbine Circuit Development and Application

To demonstrate the capability of the micro wind turbine developed in this study, we designed a micro wind turbine powered wireless motion detection system. The micro wind turbine was placed inside the HVAC air duct harvesting the energy of the air-flow. In an industrial building the air speed in the HVAC is on average 3 m/s. At this wind speed, the micro wind turbine can produce 8.02 mW of power as shown in Table 1. A wireless sensor platform can operate at power levels <1 mW (eZ430-RF2500 Development Tool 2009; Morales and Shivers 2011; Tan and Panda 2011) allowing the excess power to be accumulated in a backup storage for powering the system when there is no air flow in the duct. In order to efficiently convert power generated by the micro wind turbine it is necessary to design and implement a power converter that will allow the micro wind turbine to operate at the point of

Table 1: Summary of generator performance.

	Wind Speed	Angular Velocity (RPM)	Angular Velocity (rad/s)	AC Voltage (V)	AC Load Resistance (ohm)	AC Power (mW)	DC Voltage (V)	DC Load Resistance	DC Power
Initial	2	550	57.596	N/A	N/A	N/A	7.68	37,500	1.573
Generator	3	858	89.85	N/A	N/A	N/A	10.37	17,500	6.145
	3.7	1,097	114.88	N/A	N/A	N/A	12.84	15,000	10.99
	6	1,965	205.77	N/A	N/A	N/A	20.8	10,000	43.26
	8	2,728	285.68	N/A	N/A	N/A	26.1	7,500	90.83
	11	4,060	425.16	N/A	N/A	N/A	38.8	7,000	215.1
Final	1								
Generator	2	520	54.45	6.43	16,000	2.58	8.01	28,000	2.29
	3	817	85.56	9.81	12,000	8.02	9.76	13,900	6.85
	3.7	952	99.69	10.62	8,100	13.92	13.03	13,700	12.39
	6	1,790	187.45	19.08	6,600	55.16	21.92	9,800	49.02
	8	2,544	266.41	26.43	6,000	116.42	26.22	6,700	102.61
	11	3,703	387.78	36.8	5,000	270.85	33.72	5,000	227.41

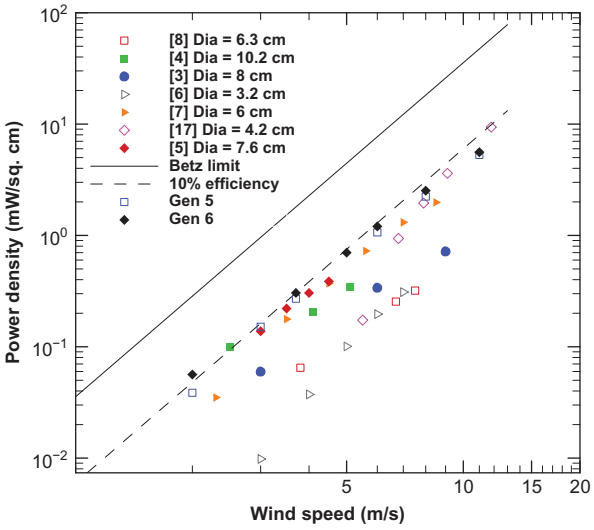

Figure 11: Performance comparison of the published micro wind turbines with the micro wind turbines developed in this study. Output power was normalized by device cross-sectional area and plotted as a function of wind speed.

maximum power. Furthermore, there is a need for energy management circuitry that will store the excess energy when available, and use it to power the rest of the system once the power output of the generator is not sufficient. The main contribution of the proposed electronic circuitry design lies in a novel approach to adapting an off-the-shelf DC/DC converter to operate with maximum power point control while retaining the high efficiency. Second contribution lies in the energy management section that is managing the power output of the micro wind turbine and the energy backup storage.

6.1 System Design

The system was designed to operate as follows: upon detection of human motion a signal was sent wirelessly to a base station connected to a computer. After relaying information about the detection the system went to a low power mode ("sleep") for a programmable period of time thus saving power. During this period, no detection of movement were performed. After the "sleep" period expired the monitoring of movement continued. During monitoring periods all parts remained in low power state except the movement detection sensor. This state was retained until the sensor detected a movement. The data received by the base station could be later used for managing the lightning conditions, controlling the temperature of the room, or any other application that requires the information on the occupancy of a room. A similar system has been reported earlier. However, it was powered by solar cells (Wahl, Milenkovic, and Amft). The proposed approach of using the micro wind turbine has a significant advantage that it can be used in places where low light levels are expected, like hallways and corridors. Based on the targeted motion detection application, four main requirements were identified for the electronics: (i) the system needed to operate over 10 years with low maintenance; (ii) movement detection sensor had to be low power; (iii) the wireless platform needed to be low power (iv) the power converter with energy management had to be placed on the back of the turbine which resulted in a size constraint 25 mm diameter circle for the printed circuit board. In order to address the lifetime requirement for the system a supercapacitor was implemented for backup storage. The motion detector is active almost continuously and therefore it was necessary to get a low power PIR detector. EKMB1303113 (Panasonic) was selected for this task because it has the current consumption <6uA when active. For the low power wireless platform the ez430-RF2500 (eZ430-RF2500 Development Tool 2009) was selected due to its low power consumption (Morales and Shivers 2011) and easy availability. The system was divided into two stages: (i) the power generation stage, consisting of the generator with the energy management, which was placed inside the HVAC duct together with the micro wind turbine; (ii) the sensing stage, consisting of the sensor with the microcontroller and the radio, placed outside the HVAC duct. The block diagram of the system is shown in the Figure 12. The separation of the power generation and the sensing stages was necessary for two reasons. First, the movement detection sensor and the radio had to be placed outside the metal air duct in order for them to work. Secondly, by incorporating the power converter and the energy management together with the micro wind turbine, a compact solution for powering low power embedded systems is produced. Such a solution could be easily used to power other applications where the wind speed is sufficient.

6.2 Power Stage

The main goal of the power stage is to keep the generator output at the maximum power point measured for 3 m/s wind speed, which is a standard in an industrial HVAC system, as well as manage the produced energy. The power stage is divided into two parts: (i) The AC/DC with maximum power point control; (ii) the energy management. Each part will be discussed in more detail in following sections.

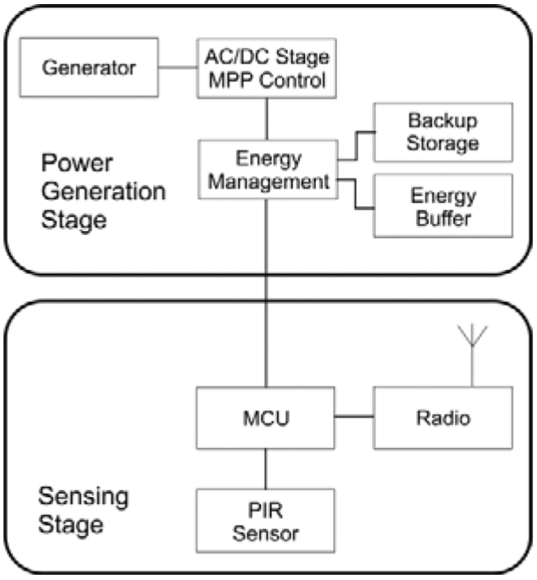

Figure 12: Block diagram of the micro wind turbine powered wireless motion detection system.

6.2.1 The AC/DC Section with Maximum Power Point Control

The AC/DC section with the maximum power point control is shown in Figure 13.

The micro wind turbine generates an AC voltage output. As the digital electronics are designed to operate using the DC voltage power supply it was necessary to rectify the turbine output. There are several options for rectification that are commonly used such as standard diode bridges, voltage doubles or active bridges. The selection of an appropriate approach depends on the input power and the voltage levels. Under the conditions that are expected in the air duct the standard diode bridge would be an efficient solution. The diode bridge used was an integrated Schottky diode bridge BAS3007

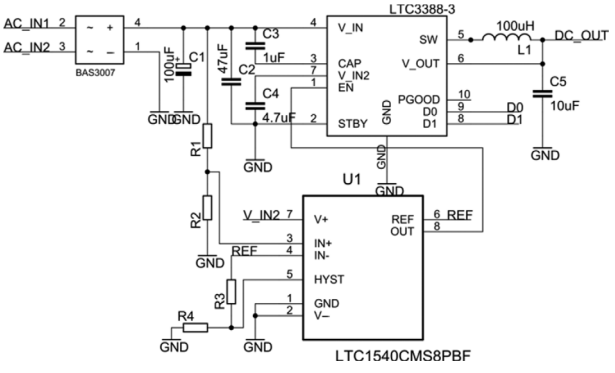

Figure 13: AC/DC stage with maximum power point control.

(Infineon Technologies). The efficiency of this diode bridge rectifier was measured to be 95% ± 1% at the wind speeds in the range of 2 m/s–3.7 m/s. With such high efficiency, it was not necessary to implement an active bridge (Tan and Panda 2011). Furthermore, an active bridge would require additional components and additional PCB real state, both of which were constrained by the design. After rectifying the output it was necessary to keep the turbine operating at a maximum power point. This is commonly done using an inductor based DC/DC converter (Friedman 2009; Kong and Ha 2012; Weddell Merrett and Al-Hashimi 2012) that emulates the optimal load. A common approach in literature is to emulate the load resistance by changing the operating conditions of the DC/DC converter. The duty cycle and/or frequency of the DC/DC converter are altered in order to achieve optimal load resistance seen by the generator. Prior researchers have usually resorted to building their own DC/DC converters in order to achieve resistance emulation. The printed circuit board area required for realization of a custom designed DC/DC converter was bigger than the area permitted by our design. As the goal was to use off-the-shelf components designing an ASIC was not an option. Therefore, we proposed a different approach where an off-the-shelf converter was controlled by activating it in short periods of time, typically several milliseconds. This mode of operation is commonly referred to as burst mode of operation.

During the active period, energy from the input capacitor is transferred using the DC/DC converter to the output capacitor. In order to keep the turbine output around the maximum power point the charging and discharging of the input capacitor are performed in a way that average voltage on the input capacitor is equal the maximum power point voltage. The amplitude of the oscillation of the input voltage, V_H, will define transfer frequency and the amount of energy transferred with each burst. Empirically it was determined that the input capacitor and V_H have to be selected in a way that will keep the DC/DC converter active at least 2 ms. Active times over 2 ms increase the DC/DC converter efficiency less than 3%. With the increase of the V_H the change of the input voltage will influence the overall efficiency because the generator will spend more time operating outside the MPP as it charges the capacitor. Based on the measurements of the power generation at wind speeds of 3 m/s, it could be calculated that for a $V_H = 0.56$ V the loss of power was 1.2% compared to power at MPP. Further increase of V_H to 1.17 V increased the loss to 2%. In applications where size of the components is important, a smaller capacitor can be used at the cost of slightly

reducing the efficiency while transferring the same amount of energy during each burst.

The DC/DC converter selected for the operation was LTC3388-3 (Linear Technology). This is a nanopower step-down converter that supports burst control. The converter was controlled by a comparator with intergraded reference LTC1540 (Linear Technology). It should be pointed out that LTC1540 was powered from a power rail used by the DC/DC converter. Based on the fact that the comparator is operating using nanowatts the LTC1540 could operate without compromising the efficiency of the converter. This was verified through a series of experiments that demonstrated no measurable change in the output efficiency between the LTC1540 controlled operation and regular operation of the converter. The LTC1540 activated the DC/DC converter once the voltage on the input capacitor reached $V_{MPP} + V_H/2$ and deactivated it when the input capacitor discharged to $V_{MPP}–V_H/2$. The resistors (R1, R2, R3 and R4) shown in Figure 13, were used to set the threshold levels as specified by the LTC1540 datasheet. The proposed circuit had fixed values for the maximum power point and hysteresis. The expected wind speeds in HVAC duct are 3 m/s, and therefore there was no need for implementing maximum power point tracking. If a change were to occur in the output power from the turbine the VMPP and VH would remain unchanged. At 2 m/s wind speed not including change in thresholds, the loss in efficiency is 9% while and 5% at 3.7 m/s. To enable maximum power point tracking, the input resistor divider R3, R4 can be substituted with circuitry from Kong and Ha (2012). Another option consists of using programmable resistors rather than fixed ones, hence providing a means of changing the V_{MPP} and V_H. The DC/DC stage efficiency at 3 m/s is shown in the Figure 14. The main objective of the DC/DC converter was to charge the buffer and storage capacitors located in the energy management section. As seen in Figure 14, during the initial stages of the capacitor charging, low energy transfer efficiencies can be expected. As the capacitors get charged, the efficiency will rise. However, as the voltage approaches the rated voltage the losses in the capacitor are growing and as a result reducing the charging efficiency. Prior researchers have reported efficiency of charging a supercapacitor of around 50% (Tan and Panda 2011). However, different capacitors have different internal structure hence direct comparison between different circuits isn't possible without using the same capacitor. Table 2 demonstrates the efficiency of charging different capacitors using the same input power of 6.63 mW (~3 m/s wind speed). The large difference between the efficiency of the 2.5 F capacitor charged to 3.3 V and 4.85 V is coming from increased losses in the super capacitor when charging to higher voltages.

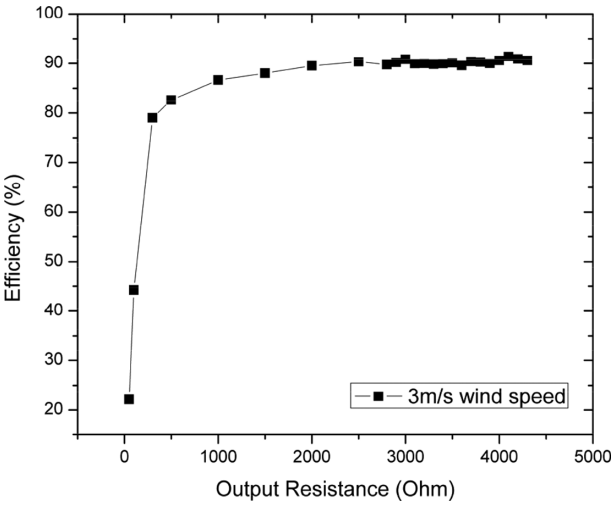

Figure 14. Efficiency of the output stage depending on the load at 3 m/s wind speed.

Table 2: Listing of components used in energy management section.

Designator	Part name	Part value
Q102, Q103, Q104	PMOS transistor	IRLML6401
Q101	NMOS transistor	FDV301N
D101, D102	Schottky Diode	BAT54
U102	Voltage Detector	MIC2779H
U101	Voltage Detector	MIC2779L

6.2.2 Energy Management

The energy management portion of the circuit enables fast startup of the sensing stage while the generator starts and stores excess energy for later use. The schematic of the energy management stage is shown in Figure 15.

The theory of operation of the energy management stage is described using the following example. Initially, the generator produces less energy than required to power the sensing stage. After this initial period, the generator begins to produce excess energy which leads to the charging of the backup storage supercapacitor, C1. When the generator stops producing power, the sensing stage continues to function using energy stored in the supercapacitor In Figure 16. The voltage waveform of the output to the sensing stage, the backup storage voltage and the energy buffer are shown to illustrate the process.

The energy management circuitry was designed to start with both the buffer capacitor C104 and the supercapacitor

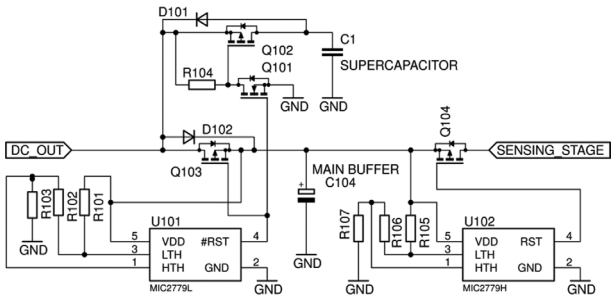

Figure 15: The schematic of the energy management stage.

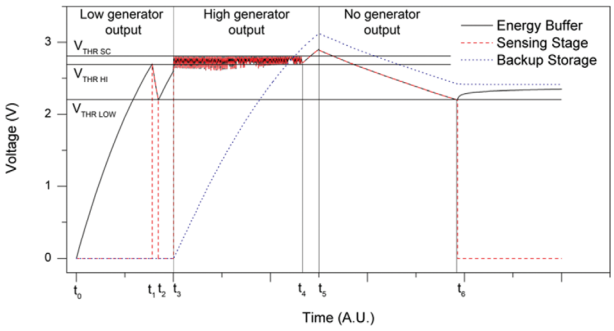

Figure 16: The voltage change on the energy buffer, supercapacitor and the output to the sensing stage.

C1 uncharged. As the turbine starts, indicated with t_0 in the Figure 16, the DC/DC converter begins to charge the buffer capacitor through D102. When the buffer capacitor reaches $V_{THR\ HI}$ of 2.7 V, at the time t_1, the sensing stage was activated. Immediately upon activation of the sensing stage the capacitor begins to discharge indicating that the sensing stage is consuming more power than the generator is producing. The sensing stage continued operation until the buffer capacitor reached the $V_{THR\ LOW}$ at the time t_2. At this point, the sensing stage was disconnected in order to prevent further discharge of the buffer capacitor as the electronics in the sensing stage cannot operate at voltages lower than 2.2 V. After disconnection, the buffer capacitor begins to recharge.

At time, t_3, the generator starts producing higher power output resulting in fast charge of the buffer capacitor to $V_{THR\ HI}$ and the sensing stage activates. However, now there is excess generated power which charges the buffer capacitor reaching $V_{THR\ SC.}$ At this point the power is re-routed from charging the buffer capacitor to charging of the backup storage supercapacitor. In the meantime the sensing stage continues to operate using the energy stored in the buffer capacitor. When the buffer capacitor fully empties to $V_{THR\ HI}$ the power gets rerouted again, interrupting the supercapacitor charging process in order to recharge the buffer capacitor. In this way the sensing stage has been given priority, thus avoiding significant discharging of the buffer capacitor.

At time t_4 the supercapacitor reaches the voltage of the buffer capacitor plus the diode voltage drop of the D102 diode, the generator starts charging both the supercapacitor and the buffer capacitor at the same time.

At time t_5, the generator stops generating power at the output and the sensing stage continues to operate by using the energy stored in the supercapacitor. There is a voltage drop of 0.3 V between the buffer and the backup storage because current always flows through either D101 or D102. When the voltage was higher than $V_{THR\ HI,}$ the D102 conducts as the supercapacitor is connected to the DC OUT, while in the other case, the diode D101 conducts as the energy buffer is connected to DC OUT net.

When the supercapacitor voltage drops below $V_{THR\ LOW}$ + 0.3 V the sensing stage is disconnected as seen at t_6. At this point, the buffer capacitor is connected to the generator, ready to be charged as energy became available. A small increase of the voltage on the energy buffer is due to the leakage currents running through the diode when the sensing stage is disconnected.

The approach of switching the output from one capacitor to another ensures that the charging process is performed as efficiently as possible. The high efficiency comes from the both capacitors being charged directly from the DC/DC converter output.

Although all components in the DC/DC stage were selected to be low power and low leakage, the DC/DC converter exhibited a higher current consumption when inactive than expected by the design. Further investigation will demonstrate the nature of this current consumption. The most likely cause is the output voltage on the DC/DC converter is higher than the input voltage. In order to reduce the current consumed by the power stage during periods when there was no wind flow, an additional PMOS transistor was placed between the DC/DC output and the input to the energy management section. The gate of the PMOS transistor was controlled from the same LTC1540 output that was used to activate the DC/DC converter. This provided a low loss connection between the DC/DC converter and the power management when the converter was active. Also it disconnected two sections when the converter was inactive. The measurements have demonstrated no change in efficiency when the additional PMOS was added to the circuit. However, the current consumption of the power management stage was reduced as shown in the Figure 17. The current flow from the backup supercapacitor was measured at different voltages.

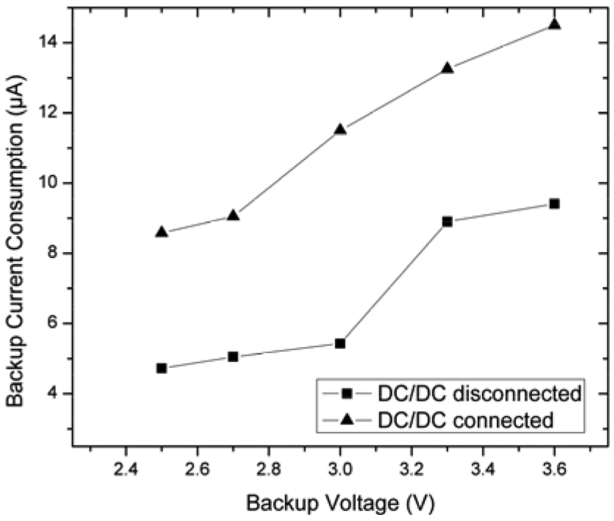

Figure 17: The power management stage current consumption comparison with the DC/DC stage connected and disconnected.

Further reduction of the power stage current consumption can be achieved by substituting the PMOS transistor drivers consisting of a NMOS with a "pull-up" resistor with CMOS drivers. The potential benefit of this can be seen in the Figure 17 where the current consumption rise at 3 V comes from the pull-up resistor on Q102 conducting. By increasing the resistor values used with MIC2779 it is possible to reduce the current consumption of the circuit. Both of these current consumption reduction approaches will be implemented in future versions of the circuit.

The list of the most important components used in this section is presented in Table 2.

6.3 The Sensing Stage

The sensing stage consisted of the ez430 board (eZ430-RF2500 Development Tool 2009) with a PIR sensor attached. The ez430 board consists of a low power MPS430 microcontroller and a CC2500 radio. The protocol used for wireless communication between the designed system and the base station connected to the computer was SimpliciTI from Texas Instruments (Friedman 2009). The microcontroller was programmed to activate the PIR sensor upon powering up and to remain in the low power regime until the sensor detects movement. Once movement was detected, the microcontroller went from low power regime into active mode and sent a packet indicating detection to the base station over a wireless link. After transmitting the packet, the PIR sensor was turned off and the microcontroller went back into low power mode for a predefined period of time. This period of time was adjustable and defined how often the movement detection would be reported. By using low power sensor platform, in conjunction with the low power PIR detector we were able to achieve the current consumption of 7 μA while monitoring for movement. High power consumption periods occurred during wireless communication of the detected movement. During these periods the radio required 17 mA to operate. However, due to the small packet sizes that need to be transmitted, the total energy needed was 130 μJ. The total average power consumption can be calculated based on the intervals between the transmissions. Figure 18 illustrates the simulated average power consumption as the function of the time system spends in the low power regime between the movement detection transmissions.

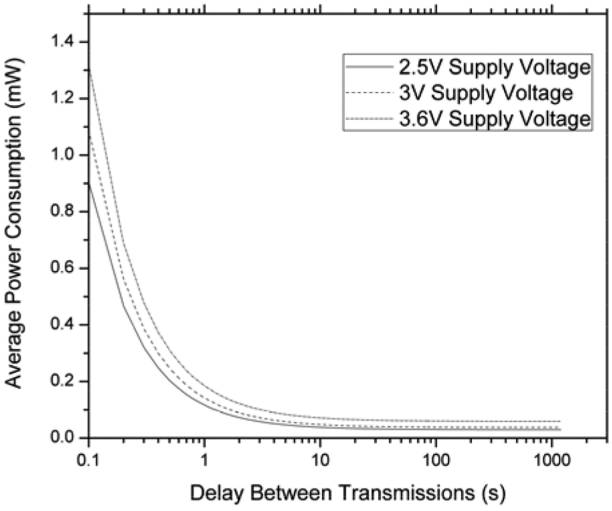

Figure 18: The average power consumption of the application as the function of the delay between detection transmissions.

In the case of our application the system was set to have a 10 min delay between movement detections. The system required 48 min of 3 m/s wind speed to charge the PHV series 2.5 F backup capacitor to 3.3 V. When powered from the previously fully charged supercapacitor the system was able to operate for 38 h. If longer backup times are required the backup supercapacitor can be charted to 5 V. In that case an additional DC/DC stage would be required between the power management and the sensing stage.

7 Conclusion

The study provides the criterion for designing and optimizing of a micro wind turbine with high system efficiency.

The importance of the coupling factor and torque/velocity relationships were investigated and applied towards the optimization of a physical prototype which sets the state-of-the-art in micro wind turbine. An electronic circuit was designed and fabricated for self-powered wireless motion detection application. We have shown a novel approach in energy management that provides high efficiency, fast startup for the wireless sensor, and energy backup for running the application when there is no airflow.

Funding: The authors gratefully acknowledge the financial support from National Science Foundation Fundamental Research Program (FRP).

References

Accessed July 28, 2013. http://energy.gov/articles/energy-department-invests-save-small-buildings-money-saving-energy.

Flammini A., and D. Marioli, et al. 2010. An Autonomous Sensor with Energy Harvesting Capability for Airflow Speed Measurements. Instrumentation and Measurement Technology Conference (I2MTC), 2010 IEEE.

Federspiel, C. C., and J. Chen. 2003. Air-powered sensor. Sensors, 2003. Proceedings of IEEE.

Xu, F. J., F. G. Yuan, J. Z. Hu, and Y. P. Qiu. 2010. Design of a miniature wind turbine for powering wireless sensors, Proc. SPIE 7647, 764741. doi:10.1117/12.847429

Howey D. A. and A. Bansal, et al. 2011. "Design and Performance of a Centimetre-Scale Shrouded wind Turbine for Energy Harvesting." Smart Materials and Structures 20:085021.

Yen Kheng, T. and S. K. Panda. 2011. "Optimized Wind Energy Harvesting System Using Resistance Emulator and Active Rectifier for Wireless Sensor Nodes." Power Electronics, IEEE Transactions on26:38–50.

Carli, D., D. Brunelli, et al. 2010. A high-efficiency wind-flow energy harvester using micro turbine. Power Electronics Electrical Drives Automation and Motion (SPEEDAM), 2010 International Symposium on, 2010.

Holmes, A. S., G. Hong, and K. R. Pullen. 2005. "Axial-Flux Permanent Magnet Machines for Micropower Generation." Microelectromechanical Systems, Journal of 14:54–62.

Burton, T. 2001. John Wiley & Sons, Incorporated.

Manwell, J. F., J. G. McCowan, and A. L. Rogers. 2006. "Wind Energy Explained: Theory, Design and Application." Wind Engineering 30:169–70.

Marin, A. 2013. Mechanical Energy Harvesting for Powering Distributed Sensors and Recharging Storage Systems. Dissertation. April 4.

Marin, A., S. Bressers, et al. 2011. "Multiple Cell Configuration Electromagnetic Vibration Energy Harvester." Journal of Physics D: Applied Physics 44:295501.

Wahl, P., M. Milenkovic, and O. Amft. A distributed PIR-based approach for estimating people count in office environments, EUC 2012: Proceedings of the 10th IEEE/IFIP International Conference on Embedded and Ubiquitous Computing

"eZ430-RF2500 Development Tool". 2009. Texas Instruments, Inc.

Morales, M., and Z. Shivers 2011. "Wireless Sensor Monitor Using the eZ430-RF2500", Texas Instruments, Inc.

Tan, Y. K., and S. K. Panda. 2011. "Optimized Wind Energy Harvesting System Using Resistance Emulator and Active Rectifier for Wireless Sensor Nodes." IEEE Transactions On Power Electronics 26:38–50.

Weddell, A. S., G. V. Merrett, and B. M. Al-Hashimi. 2012. "Photovoltaic Sample-and-Hold Circuit Enabling MPPT Indoors for Low-Power Systems", IEEE Transactions On Power Electronics, 27:1196–1204.

Kong, N., and D. S. Ha. 2012. "Low-Power Design of a Self-powered PiezoelectricEnergy Harvesting System With Maximum PowerPoint Tracking." IEEE Transactions On Circuits And Systems–I: Regular Papers, 27:2298–2308.

Friedman, L. 2009. SimpliciTI: Simple Modular RF Network Specification. San Diego, California USA: Texas Instruments, Inc.